Niobium as an alternative cladding material for neutron producing targets: Analysis of erosion response

MADHUWANTHI, H.M.L.U. <http://orcid.org/0000-0003-1008-7261>, PURANDARE, Yashodhan <http://orcid.org/0000-0002-7544-9027>, EHIASARIAN, Arutiun <http://orcid.org/0000-0001-6080-3946>, DEY, A., JONES, L. and GALLIMORE, S.

Wear 580–581 (2025) 206291

Contents lists available at ScienceDirect

Wear

journal homepage: www.elsevier.com/locate/wear

Niobium as an alternative cladding material for neutron producing targets: Analysis of erosion response

H.M.L.U. Madhuwanthi [a,*], Y.P. Purandare [a], A.P. Ehiasarian [a], A. Dey [b], L. Jones [b], S. Gallimore [b]

[a] School of Engineering and Built Environment, National HIPIMS Technology Centre, Sheffield Hallam University, City Campus, Howard Street, Sheffield, S1 1WB, United Kingdom
[b] Rutherford Appleton Laboratory, Didcot, OX11 0QX, United Kingdom

ARTICLE INFO

Keywords:
Erosion mechanisms
Impinging jet slurry erosion
Cavitation erosion
Niobium

ABSTRACT

The current design of neutron producing spallation targets (TS2) at ISIS constitutes a Tungsten (W) core cladded with a thin Tantalum (Ta) sleeve which facilitates circulation of cooling water. These targets are undergoing premature failure due to erosion-corrosion of the Ta sleeve as one of the primary causes. This has drawn attention towards sourcing alternative cladding materials and Niobium (Nb) is potentially seen as a candidate. However, the aqueous slurry erosion response of Nb is unreported and needs scrutiny. In this work, slurry erosion performance of Nb was studied with the help of an impinging jet erosion-corrosion apparatus. Aims included measuring erosion rate of Nb with respect to abrasive particle concentration, slurry velocity, and slurry impingement angle including determining erosion mechanisms. Results revealed peak erosion rate at a slurry impingement angle of 30°, and for velocities of 6 ms^{-1} having a particle concentration of 7 wt%. The material removal mechanism involved a dominating ploughing and type-1 micro-cutting action at shallow angles of impact as compared to formation and breakage of platelets due to a 'plastic deformation-fatigue' dominated wear mechanism at near normal impact angles. The erosion response of Nb thus could be described as one typically observed for ductile materials. Experiments were also performed to analyse the cavitation erosion resistance of Nb using an ultrasonic vibratory apparatus (sonotrode) in de-ionised water to complement impinging slurry jet studies.

1. Introduction

Neutron beam analysis is a high precision technique to reveal the atoms, molecules, and crystallographic structure of broad range of materials, which requires large-scale facilities such as the ISIS Neutron and Muon Source based at Rutherford Appleton Laboratories (RAL). Various spallation target designs employed around the world mostly consist of a heavy metal such as tungsten (W) which forms the neutron producing core [1]. Due to the decay heat of irradiation, the spallation target reaches temperatures of around 250 °C and needs to be continuously water cooled to prevent temperature build up. The TS2 spallation target (source) design at ISIS consists of a tantalum (Ta) clad tungsten core [2]. The Ta cladding is Hot Isostatic Press (HIP) bonded to the core and acts as a barrier separating the cooling water and the electrochemically weaker W core. The spallation target is expected to last for 5 years of continuous use under routine operating conditions, however premature failure of this target (TS2) under two years is causing operational and economic losses. Damage caused by erosion-corrosion of the Ta sleeve is estimated to be one of the primary causes of this premature failure along with other possible mechanisms such as thermal stresses and radiation damage [2].

Erosion-corrosion, a form of tribocorrosion, can be defined as the progressive loss of material due to the action of abrasive particles under corrosive conditions [3]. The extent of loss is governed by complex material removal mechanisms of the material(s) involved, in turn influenced by its mechanical properties, corrosion response along with their interaction with each other. It is also influenced by various factors, such as impact conditions (impact velocity and angle), erodent particle properties (hardness, shape, and size), and fluid properties (density, temperature, pH, and viscosity). In most instances, the interaction is synergistic and leads to enhanced wear of the material than their mathematical sum [3]. Cooling water circulation analyses at the TS2

* Corresponding author.
E-mail address: L.Herath-Mudiyanselage@shu.ac.uk (H.M.L.U. Madhuwanthi).

https://doi.org/10.1016/j.wear.2025.206291
Received 7 March 2025; Received in revised form 7 August 2025; Accepted 11 August 2025
Available online 11 August 2025

station in RAL have shown falling pH values with time and traces of W^+ isotopes in the cooling water loop which speculatively have been attributed to the formation of tribocorrosive conditions [2]. With this backdrop, tribological studies on pure Ta conducted previously have demonstrated that its erosion resistance is highly dependent on the impact angle [4], and that corrosion protection offered by Ta is severely diminished by erodent particle bombardment due to the removal of the protective passive layers [5]. With this accrued knowledge, the Ta sleeve is envisaged to eventually suffer structural destruction due to erosion-corrosion, thereby accelerating corrosion of the W core. Thus, a significant motivation exists to find an alternative cladding material to replace Ta.

Niobium (Nb) belongs to the group of transition metals which have a high melting point, high elevated temperature mechanical properties, high thermal conductivity, and high corrosion resistance [6]. Due to its extraordinary properties, Nb has been used as a key alloying element in production of steels with enhanced high temperature mechanical properties and corrosion resistance and for the production of superalloys [7]. Along with these superior properties, low density, high ductility at low cryogenic temperatures and high temperature creep resistance has enabled Nb based alloys to be a favourable choice for space industry and nuclear reactors [8,9]. In its pure form, Nb can resist neutron embrittlement and has a very low neutron absorption cross section [10,11]. Thus, Nb presents itself as an alternative cladding material. However, the suitability of Nb to resist tribocorrosion is yet to be analysed. The slurry erosion response of pure Nb is unreported and a very limited literature on its Cavitation Erosion (CE) can be found [12]. CE wear is caused by the damage of the surface and the loss of mass due to the impacts caused by the collapse of bubbles and the shock waves generated by it. In the case of metals with considerable ductility such as stainless steels, the grains undergo plastic deformation (undulations) until resisted/arrested by the grain boundaries, slip bands or inclusions. This leads to stress accumulation/strain hardening which is then followed by fatigue cracking due to the continuous and cyclic impact loading of the shock waves from the collapsing bubbles [13–15]. Studies on CE of Nb have demonstrated similarities to the CE behaviour of untreated stainless steel wherein microcrack formation followed by fracture of grains due to fatigue have been reported as the main material removal mechanism [12]. Although CE studies tend to produce a general understanding of erosion (less control over impact velocities of microjets and stress pulses generated due to microbubble collapses), slurry impinging jet erosion studies help to reveal the effect of impact velocities, impact angles, and particle concentration under greater control and thus can form a more detailed input for design considerations.

This work mainly focuses on aqueous impinging slurry jet studies on Nb with the overarching aim of identifying material removal mechanisms under particle bombardment conditions in the absence of corrosive conditions. Experiments have been performed at different slurry jet velocities, impact angles, and particle concentrations. CE erosion experiments have also been performed to aid additional and comparative discussions. Results from this study will immensely contribute towards understanding the erosion-corrosion response and suitability of Nb for cladding applications as well as towards the design of future target materials at ISIS.

2. Materials and methods

Nb specimens were produced by sectioning an annealed Nb rod which had a purity of 99.8 wt% (supplied by Goodfellow Cambridge Limited, England) into circular discs (30 mm diameter and 5 mm thick). These discs were then metallographically polished to a mirror finish using various grades of abrasive paper and polishing pads followed by a final polishing step using colloidal silica.

Prior to the slurry erosion experiments, microstructural aspects of Nb specimens were analysed using X-Ray Diffraction (XRD), X-Ray Fluorescence (XRF), and Vickers micro-hardness techniques. An Empyrean diffractometer (Malvern Panalytical, the Netherlands) was used to obtain the XRD results (Co-Kα x-ray source, $\lambda = 1.79$ Å) using the Bragg-Brentano geometry (2θ = 5–140°) with a step size of 0.0001°. The elemental purity of the Nb specimens was determined by using a Primus IV XRF spectrometer (full x-ray spectrum of Rh source). Indentation hardness was measured using a Duramin Stuers-40 AC3 Vickers micro-hardness tester. A major load of 4 kgf with a dwell time of 10 s was chosen after conducting load optimisation trials. A nanoindenter (Anton Parr-CSM instruments, Switzerland) with a Berkovich tip and a maximum load of 400 mN was used to measure the Young's modulus values.

Slurry erosion experiments were conducted with the help of a homebuilt aqueous impinging jet erosion-corrosion apparatus, details of which can be found in previous publications [4,16]. The distance between exit nozzle and the specimen surface was maintained at 15 mm while the experiments were conducted at ambient temperatures (22–24 °C). Slurry jet was made incident on a fixed exposed area (circular area of 0.28 cm^2) whereas the rest of the specimen was masked using a masking lacquer and a cover sleeve. Preliminary experiments were performed with respect to a number of erosion parameters that would lead to measurable mass loss in accelerated laboratory conditions consisting of stipulated time of 1 h. Hence slurries used in this study constituted a mixture of irregular shaped silicon carbide (SiC) particles with a hardness value in the range of 25 GPa, mean size range of 500–700 μm and deionised water.

In order to prevent build-up of temperature, the TS2 spallation target is cooled with the help of a closed loop system which circulates deionised water with velocities ranging from 4 to 12 ms^{-1}. Thus, the current study primarily focused on investigating the slurry erosion behaviour of Nb specimens at the intermediate velocities of those used for cooling the TS2 target. In order to identify the effect of particle concentration, experiments were performed by varying the particle concentration (3, 5, 7, and 9 wt%) while keeping the constant velocity at 6 ms^{-1}. In this study, a larger diameter exit nozzle (6.5 mm) was used to achieve 3 wt% slurry concentration, whereas a smaller diameter exit nozzle (6 mm) was used for the remaining three concentrations (5, 7 and 9 wt%) while keeping the inlet nozzle constant [17]. Correspondingly, the unmasked area undergoing particle bombardment on the specimen also increased with the exit nozzle diameter. Similarly, to analyse the effect of slurry velocity, experiments were performed at different slurry velocities (5, 6, and 7 ms^{-1}) at constant particle concentration. Then studies were extended to find the effect of impact angle on peak erosion rate, experiments were performed at different slurry jet impact angles (20, 30, 45, 60, and 90° relative to the plane of the specimen) while maintaining a constant slurry concentration of 7 wt% and velocity of 6 ms^{-1}. The results of these preliminary experiments were used to determine the experimental parameters to be used for analysing erosion mechanisms with an overarching aim of using the most aggressive conditions.

After erosion experiments, specimens were carefully rinsed using deionised water and then dried using a handheld air dryer. An analytical balance (Ohaus PA114C, Fisher Scientific, UK) which has an accuracy of 0.0001 g was used to measure the mass of the sample before and after experiments (without mask). All impinging jet slurry experiments were conducted for 1 h and repeated 3 times to calculate error margins using the standard deviation method. The slurry erosion rate was calculated in gg^{-1}, as the ratio of the mass of material removed in gs^{-1} to the mass of erosive particles striking the surface in gs^{-1}. Erosion rate normalised to unit area ($gg^{-1}cm^{-2}$) have been reported to demonstrate the effect of particle concentration and to compare erosion results of Ta reported in the article [4]. This approach helps to negate the effect of changing cross-sectional area of the jet with respect to the exit nozzle employed to achieve the respective particle concentration and velocity combination.

CE experiments were performed in distilled water at ambient temperatures using an ultrasonic cavitation device (UIP 1000 hdt, Hielscher Ultrasonics GmbH, Germany) equipped with an 18 mm diameter titanium sonotrode. Longitudinal oscillation of 20 kHz at a peak-to-peak

amplitude of 50 μm was used to induce cavitation effects on the Nb disk specimen which was placed at a distance of 1 mm from the horn. Cumulative mass loss was measured at 15-min intervals for the first 60 min, followed by 30-min intervals until the total testing time reached 180 min. These experiments were repeated for 3 times to get a general idea of the cavitation erosion response of Nb.

Erosion scars generated at an impact angle of 30° and 90° and CE scars were imaged using a Scanning Electron Microscope (SEM) in the Secondary Electron (SE) imaging mode (FEI Quanta 650 and NovaNanoSEM200, ThermoFisher Scientific, The Netherlands) to identify the material removal mechanisms.

3. Results and discussion

3.1. Characterization results

Fig. 1 shows the results from the Brag Brentano test. As evident, the specimen had a highly crystalline body-centered cubic (b.c.c.) structure (ICCD powder diffraction file, PDF: 00-035-0789). The relative intensities of (110), (211), and (220) orientated grains were consistent with randomly oriented powder material. XRF studies confirmed that the Nb specimens had a purity of 99.8 % with trace amounts of silicon (Si), sodium (Na), and iron (Fe) (<0.2 %). Indention hardness of Nb was found to be 69 ± 0.5 HV and whereas the Young's modulus value was 104 ± 3.2 GPa.

3.2. Slurry-erosion experiments

In this study, a number of preliminary slurry erosion experiments were performed to identify parameters which would yield accelerated erosion of Nb. These mainly consisted of the effect of impact angle, particle concentration and impact velocities.

3.2.1. Slurry impingement angle

To analyse the effect of impact angle, an experimental matrix consisting of 5 different slurry impingement angles (jet incident on the surface of the specimen) was chosen. These were namely 20, 30, 45, 60, and 90° whereas an intermediate impact velocity of 6 ms^{-1} and concentration of 7 wt% were chosen and held constant for these experiments. Fig. 2 exhibits the results obtained.

As evident from Fig. 2, the slurry impingement angle had a strong influence on the erosion rate of Nb. Erosion rate calculated for the impact angle of 20° was 4.8 × 10^{-9} gg^{-1} and it increased to 13.0 × 10^{-9} gg^{-1} for 30° which eventually culminated as the peak erosion rate. Further increase in impact angle led to a gradual but consistent drop in the erosion rate. The lowest erosion rate was found to be at normal impact (3.5 × 10^{-9} gg^{-1}) which was about 3.7 times lower than that observed for impact angle of 30° and indeed lower than measured for

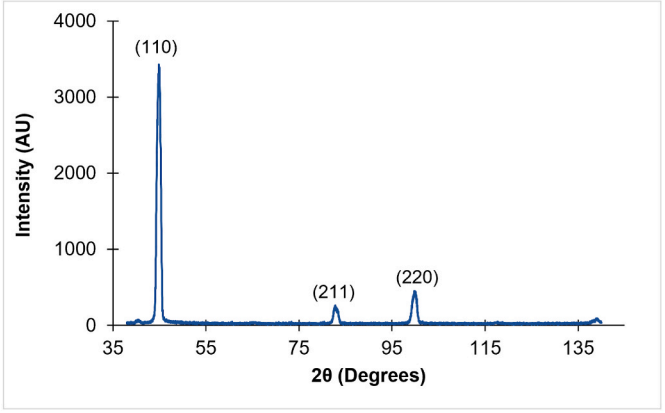

Fig. 1. X-ray diffractogram of Nb sample.

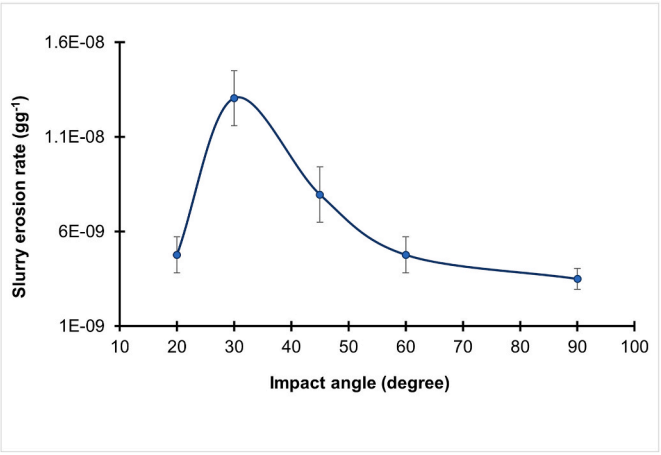

Fig. 2. The slurry-erosion dependence of Nb samples with impact angle.

impact angle of 20°. This behaviour can be described as one typically observed for ductile materials attributed to the difference in material removal mechanisms acting at different impact angles [18]. There is a consensus among researchers [18–20] that for ductile metals, material removal is based on the detachment of the displaced material (lips) which undergo further plastic deformation with subsequent particle impacts thereby undergoing work hardening effect. These strained lips eventually fracture due to fatigue causing mass loss. Thus, the material is removed through a "plastic deformation-fatigue" process. For steeper impact angles (near normal angles), plastic deformation is localised around the indent caused by a particle impact [18–21] thus reducing the mass removal rate.

In comparison, at shallower impact angles several mechanisms such as ploughing, type-1 cutting and type-2 cutting participate in material removal. In ploughing mode, material pile up occurs in the front and sides of the indent mostly throughout particle trajectory on the surface [18]. This strained material is then dislodged upon following impacts [22]. Type-1 and type-2 contributions depend on the shape (sharpness) of the erodent particles and their interaction while moving along the surface [18]. Thus, ductile metals erode at a higher rate at shallower impact angles. Nb exhibited similar material removal mechanisms with respect to impact angle as described above (and explained further in section 3.2.4) and thus a typical ductile behaviour [4,23].

3.2.2. Slurry concentration

In this study, the effect of particle concentration was analysed by conducting experiments at two impact angles; namely at 30° and 90° which corresponded to the peak erosion rate and the lowest erosion rate of Nb respectively. The velocity was held constant at 6 ms^{-1}. Fig. 3(a) and (b) show the results of this study.

As observed, the concentration of 7 wt% yielded the peak normalised erosion rates ((4.66 ± 0.82) x 10^{-8} $gg^{-1}cm^{-2}$ for 30° and (1.25 ± 0.31) x 10^{-8} $gg^{-1}cm^{-2}$ for 90°). As the concentration was lowered to 5 wt %, normalised erosion rates also exhibited a drop ((3.18 ± 0.62) x 10^{-8} $gg^{-1}cm^{-2}$ for 30° and 0.74 × 10^{-8} $gg^{-1}cm^{-2}$ for 90°). However, a deviation from expectation was observed when the concentration was further lowered to 3 wt% resulting in a higher erosion rate as compared to 5 wt% for both impact angles ((4.32 ± 0.54) x 10^{-8} $gg^{-1}cm^{-2}$ for 30° and (1.08 × 10^{-8} $gg^{-1}cm^{-2}$ for 90°). A deviation from the expected trend was also observed for erosion rates for 9 wt% concentration which yielded the lowest erosion rates in this study ((2.25 ± 0.54) x 10^{-8} $gg^{-1}cm^{-2}$ for 30° and (8.25 ± 3.12) x 10^{-9} $gg^{-1}cm^{-2}$ for 90°). Experiments conducted at impact angle of 30° yielded a higher erosion rate for particular concentration as compared to the experiments performed at impact angle of 90°. In general, SiC concentration of 7 wt% in the slurry yielded peak erosion rates for both angles.

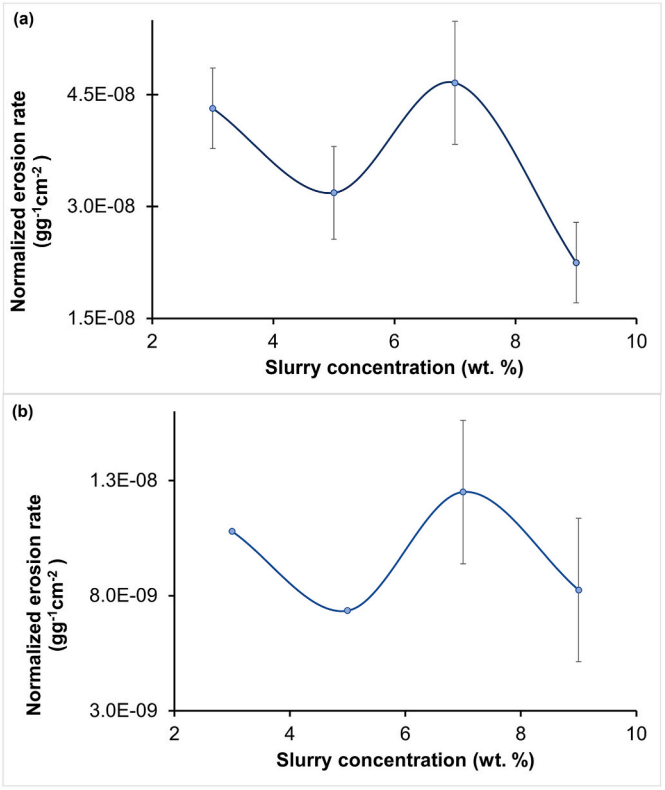

Fig. 3. Erosion rate normalised to unit area of Nb against the slurry concentration at a constant velocity of 6 ms^{-1} and impingement angle of (a) 30° and (b) 90°.

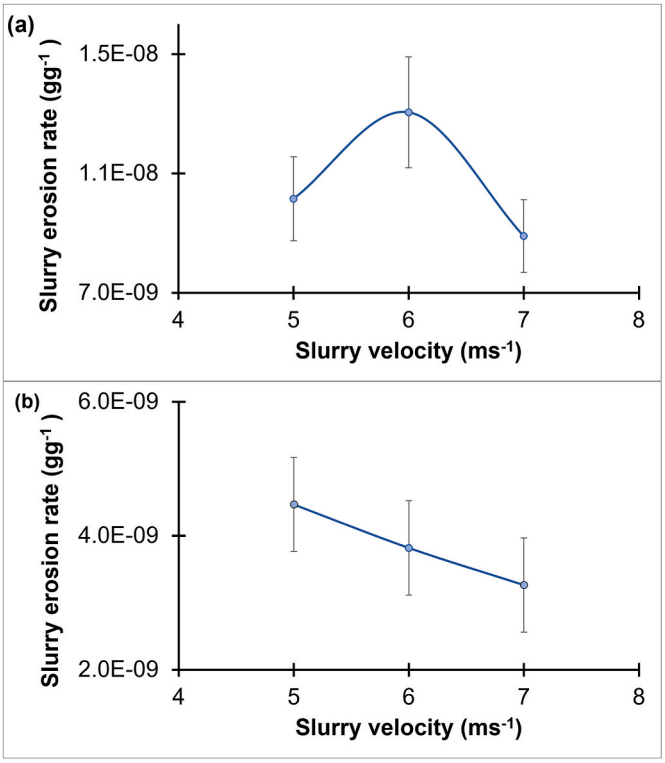

Fig. 4. Erosion rate of Nb against the slurry velocity at a constant slurry concentration of 7 wt% and impingement angle of (a) 30° and (b) 90°.

There is a general consensus that erosion rate is proportional to the mass of erodent particle incident on the surface [22]. The SiC particles used in this study had a hardness value in the range of 25,500 MPa (approximately 2500 HV) which was several times (36 times) harder than Nb (69 HV). Thus, it is safe to estimate that erodent particles did not disintegrate upon impact and get embedded on the Nb specimen (also evident from several SEM images gathered in this study) and thus did not lead to any incubation behaviour caused by weight gain.

In this study, a larger diameter exit nozzle was used to achieve 3 wt% slurry concentration. Thus an "increase" in erosion rate for 3 wt% concentration can be attributed to a higher mass of erodent particles incident on the surface [24]. Concurrently, a drop in the erosion rate for 9 wt% concentration could be attributed to the "particle shielding" effect wherein some particles near the surface hinder the contact of subsequent approaching particles with the surface leading to an inter-particulate collision between rebounding and incoming particles rather than participating in material removal [25]. These inter-particulate collisions cause dissipation of the initial kinetic energy of the erodent particles and hence a reduction in incoming particle's velocity as well as alteration of impact direction. The "shielding effect" appeared to be consistent for both impact angles studied (30° and 90°).

3.2.3. *Impact velocity*

Fig. 4(a–b) show the erosion rate obtained for impact angles of 30° and 90° with respect to changing impact velocity. The erodent particle concentration was held constant at 7 wt%. It can be observed that the highest erosion rate for impact angle of 30° was obtained for an impact velocity of 6 ms^{-1} which was almost one order of magnitude higher ((1.30 ± 0.19) x 10^{-8} gg^{-1}) as compared to 5 ms^{-1} ((1.02 ± 0.14) x 10^{-8} gg^{-1}) and 7 ms^{-1} ((0.89 ± 0.12) x 10^{-8} gg^{-1}). The effect of velocity on erosion rate obtained for impact angle of 90° was very unclear, the three velocities studied here exhibited values of (4.47 ± 0.70) x 10^{-9} gg^{-1} (5 ms^{-1}), (3.82 ± 0.70) x 10^{-9} gg^{-1} (6 ms^{-1}), and (3.26 ± 0.70) x 10^{-9} gg^{-1} (7 ms^{-1}). In general, erosion rates obtained at 30° were an order of magnitude higher than those obtained for incident angle of 90°.

A shielding effect, as explained above, could be responsible for the drop in erosion rate observed for higher impact velocity of 7 ms^{-1} as compared to 5 and 6 ms^{-1} as higher velocities lead to higher number of particles approaching the surface. Although this effect was more evident for impact angle of 30°, lower material removal rates at normal impact angles in general meant that mass loss measured had a wider error leading to almost similar erosion rates for all three velocities employed in this study (Fig. 4(b)).

3.2.4. *Erosion mechanisms*

The results from preliminary experiments on the effect of impact angle, erodent concentrations and impact velocities were utilised to determine parameters for investigating the erosion mechanisms of Nb. Accordingly, the parameters which resulted in the most aggressive conditions in this study, i.e. impact velocities of 6 ms^{-1} and SiC concentration of 7 wt% were chosen. Shallow impact angle of 30° (peak erosion rate) and normal impact angle (least erosion rate) were chosen in particular to identify the difference in erosion mechanisms. It is envisaged that the material removal mechanism at intermediate impact angles (30°–90°) will consist of a mix of these mechanisms with varying contributions.

Fig. 5(a) shows the angular SiC particles with the sharp edges whereas Fig. 5(b) shows the surface topography of the Nb specimen after the mirror finished stage. Fig. 5(c) and (d) show the erosion scar generated under the shallow impact angle of 30° at low magnification and higher magnification, respectively. As expected, the surface of the Nb specimen appeared very rough owing to the damage caused by the impact from the irregular shaped SiC particles. Features resembling hills and valleys could be observed as craters and plastically deformed lips surrounding these craters resulting from the micro-ploughing action of impacting particles dominated the topography. These lips/platelets

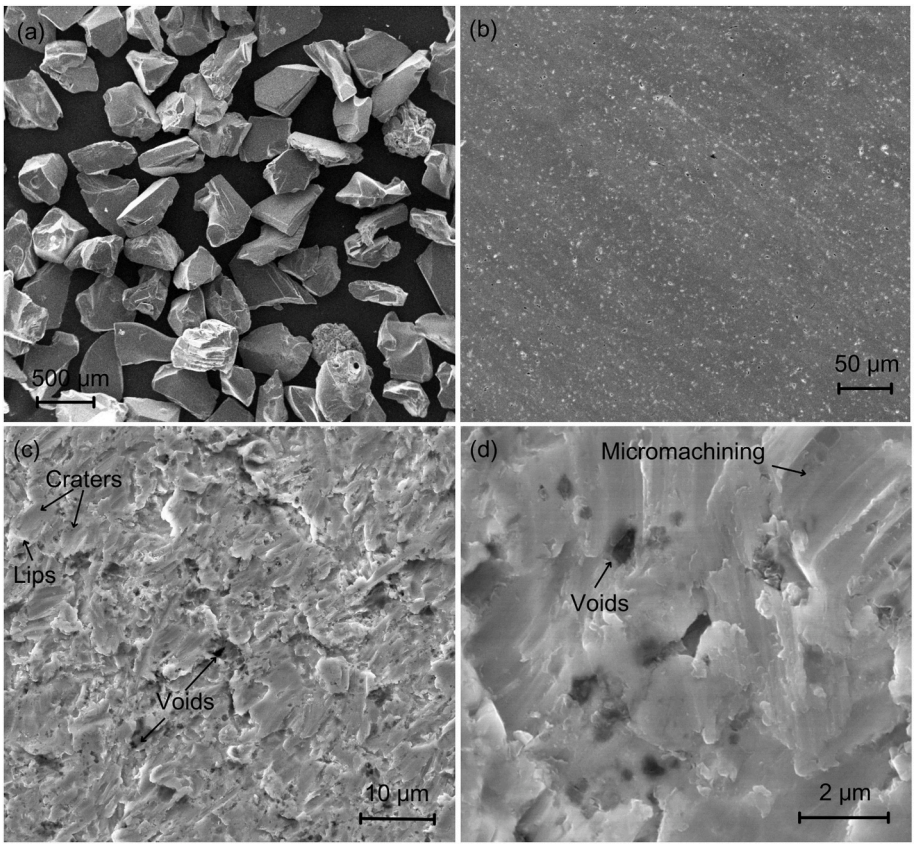

Fig. 5. (a) SiC carbide particles used in this study (b) mirror finished Nb surface before tests, erosion scars formed under 30° impact: (c) low magnification (d) perforation and lip breakage visible at higher magnification.

appeared flattened and extensively deformed (akin to smearing due to impact extrusion) along the direction of particle impacts. The erosion scars also exhibited abundant scoring marks, micromachining marks and abrupt breakage of flattened lips (bright areas visible in the SEM images in Fig. 5(c) and (d)). Localised perforation of thin extruded lips was prominently visible at higher magnification (circular voids all over the eroded surface in Fig. 5(c) and (d)) along with some grain boundary cracking at few places (Fig. 7(a)).

Fig. 6(a–b) show the erosion scars obtained under a normal impact angle. As observed for 30° impact, the surface appeared rough and filled with features resembling plastically deformed, but flattened lips which were abruptly broken at few places. Indentation perforation on these extruded lips was also clearly visible and were found evenly distributed all over the scar. However, a stark difference was the absence of scoring or micromachining marks, and the directional deformation (smearing) of the platelets/lips as compared to the scar obtained for 30° impact angle. Grain boundary cracking was also visible (Fig. 7(d)). In general, formation of indention platelets or lips and flattening of these lips due to subsequent particle impacts were dominantly visible for the erosion scars at normal impact angle. Importantly, embedment of erodent particles, either full or broken fragments, was not observed for any of the erosion scars when analysed under the SEM and hence can be considered negligible for both impact angles.

The erosion is a process of accumulation of numerous single erodent particle impact events and can include several mechanisms of material removal acting simultaneously. In order to resolve them, experiments

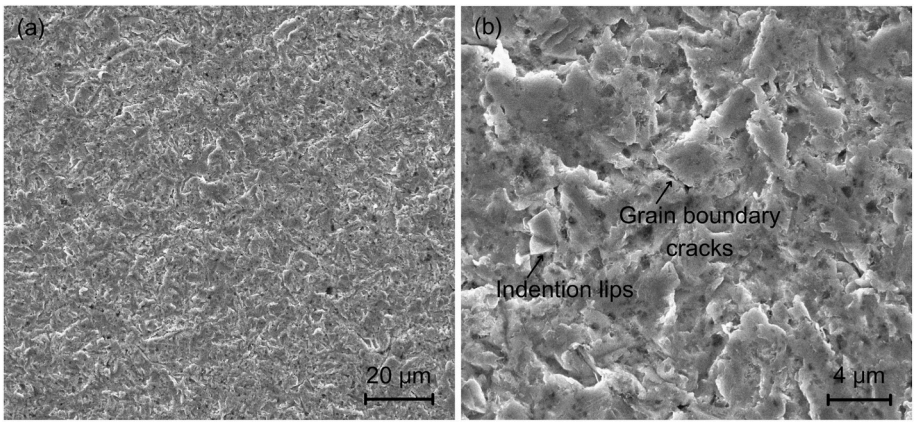

Fig. 6. Erosion scars formed under 90° impact: (a) low magnification (b) perforation and lip breakage visible at higher magnification.

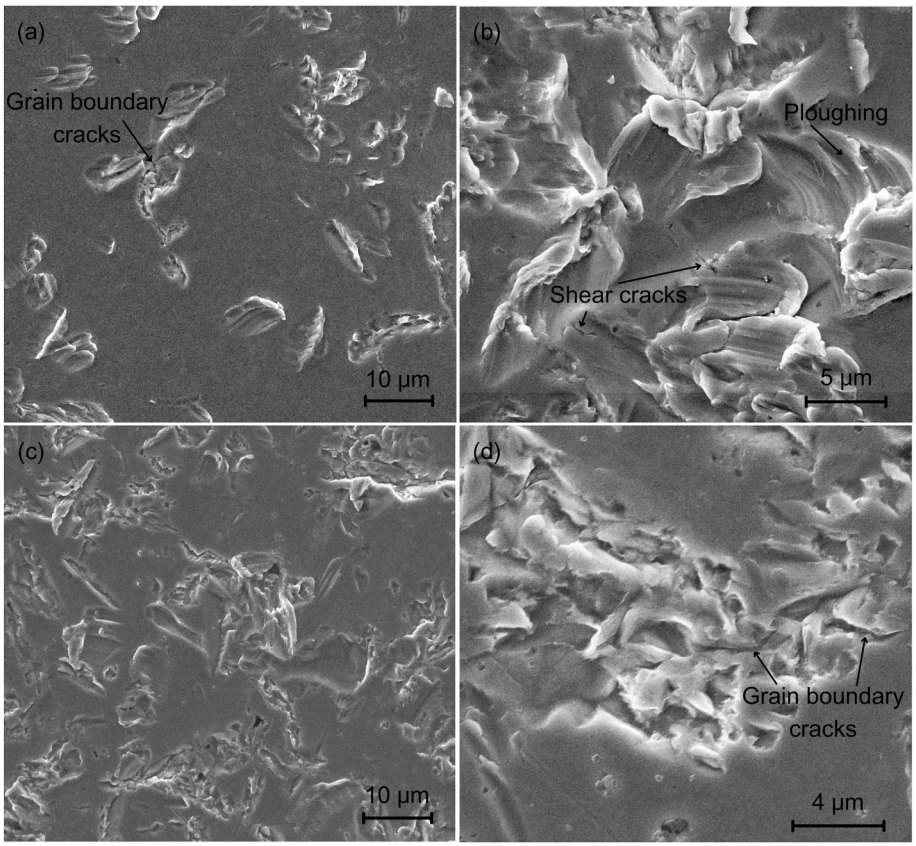

Fig. 7. SEM images; (a–b) surface artifacts created after fewer impact events at 30°and (c–d) after fewer impacts at 90°.

were also performed under fewer particle impacts. Fig. 7(a–b) and (c-d) show the SEM images of the mirror polished surface which underwent fewer SiC particle impacts at the 30° and 90°, respectively.

As observed in Fig. 7(a–b), cutting mechanisms such as ploughing and type-1 cutting were prominently present and material pile-up (lips) around the craters was evident. Some grain boundary cracking (Fig. 7 (a)) and shear cracks (Fig. 7(b)) were also observed at the site of impact. Considering the smoother finish of the flattened platelets in general (Fig. 5(c)) it can be speculated that type-2 cutting action due to the rolling or dragging of the erodent particle during interparticle collisions may have also contributed to material removal. These results suggest that ploughing and type-1 cutting action along with perforation of the thin extruded lips due to particle indentation (leading to lip breakage) and grain pull out due to cracking predominantly contributed to the material removal mechanism for 30° impact angle.

Fig. 7(c–d) show the impact craters created after particles impinged at impact angle of 90°. The indents appear deeper albeit with limited material pile-up surrounding them whilst some grain boundary cracking was also evident. Thus, material removal at normal impact proceeded through lip breakage and grain pull-out mechanisms. Unlike cutting wear at shallow angles, wear at a normal impact angle is a cumulative process of plastic deformation of the fragments until reaching the localized critical strain, followed by fatigue fracture [19].

In general, pure metals show a good inverse co-relation between hardness and erosion rates for annealed pure metals [26]. The SiC particles used in this study had a hardness in the range of 25 GPa (2200–2600 HV) which was considerably higher than the hardness of Nb (69 ± 0.5 HV) used in this study. Hence any effect of impact on the bombarding particles, apart from breakage of sharp corners, can be neglected. XRD results of Nb revealed that the specimens had a b.c.c crystal structure with a crystallite size of 598 ± 200 Å with a dominating (110) orientation of the grains. The average grain diameter (obtained from SEM studies) was found to be 22.4 ± 4.3 μm. The erosion mechanisms (material removal) identified in this study mainly constituted plastic deformation followed by fatigue fracture and micro-cutting. Thus, the mechanical properties of Nb such as hardness (resistance to indentation/plastic deformation), ductility (critical strain for detachment), toughness (ability to absorb impact energy), Young's modulus and work hardening rate will play a crucial role in determining the damage and mass loss [26].

3.3. Comparison with respect to Ta

Fig. 8 compares slurry erosion results of Nb (from this study) with those reported for Ta previously [4] and presents a good qualitative

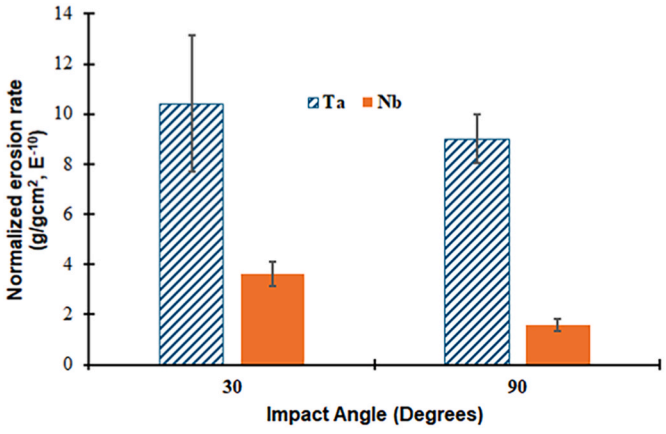

Fig. 8. Comparison of slurry erosion rates of Nb and Ta. Values of Ta were obtained from previous studies reported in reference 4.

overview of the erosion behaviour. The comparison is based on the erosion rates at two impingement angles (30° and 90°) wherein all other experimental parameters employed such as impact velocity (5 ms^{-1}), particle concentration (7 % wt.), distance from the exit nozzle etc. were similar. Both, Nb and Ta exhibited a ductile erosion behaviour and the material removal mechanisms were found to be similar with micro-cutting and ploughing dominating at shallower impact angles and 'plastic deformation-fatigue breaking' at near normal impact angles. As observed, the erosion for Ta was 2.9 times and 5.6 times higher at an impact angle of 30° and at 90° respectively as compared to Nb for the conditions employed. This is significant, since Ta had a higher hardness value (89 ± 3 HV) as compared to Nb (69 ± 0.5 HV). Even though the crystal structure of both metals was similar, Ta specimens were manufactured through powder metallurgical route whereas Nb specimens were in an annealed state and could be attributed to the difference in erosion rate observed.

3.4. Cavitation erosion response

Fig. 9(a) presents the cumulative mass loss measurements recorded as a function of erosion time, whereas Fig. 9(b) presents the erosion rate (cumulative mass loss per minute, $gmin^{-1}$) calculated for the Nb specimen. As evident, the incubation period of Nb was in the range of 35–40 min, after which the mass loss increased gradually with time until the end of test. The four stages of cavitation erosion response [12] of Nb, i.e. the incubation stage (0–40 min), acceleration stage (40–90 min), maximum erosion rate stage (90–120 min) and deceleration stage (120–180 min) can be clearly identified in Fig. 9(b).

Fig. 10(a–d) show the damage caused by the CE tests with respect to cumulative test time. The specimen showed the onset of micro-undulations due to local plastic deformation and small extent of micro-pitting in the incubation stage (Fig. 10(a)). The severity of the undulations, i.e. extent of plastic deformation increased as the test time progressed (45 min) resulting in grain boundary sliding. As a result, the grain boundary network was clearly exposed amid some degree of vertical dislodgment of grains. The sizes of the pits also increased, although the number of pits did not rise dramatically as evident from the SEM studies, Fig. 10(b). A large extent of intergranular as well as trans-granular cracking was also evident, and the interiors of the pits showed fatigue striations (observed at a higher magnification, Fig. 11 (c)) following the breakage of the grain(s).

As the test time reached 60 min, the surface appeared heavily damaged and most of the grains in the test area underwent fatigue breakage (clear fatigue striations visible) with deeper pits evident at a number of places (Fig. 10(c)). As the test time exceeded 150 min, the damage from grain breakage was extensive as it formed deeper and deeper voids as a result of progressive and coalesce of material removed from the damage sites.

CE erosion, Fig. 11(a), shows void created at the end of 45 min of test duration which approximately falls around the end of incubation period. The void formation is visible possibly at the junction of few plastically deformed grains which have been vertically dislodged (resulting from the undulations). Along with the void, intergranular and trans-granular cracks were also visible. The bottom of the pit clearly shows fatigue striation marks which suggested that the surface work-hardened and the deformed grain(s) fractured due to fatigue owing to the cyclic loading nature of the CE tests.

Fig. 11(b) shows the area of the specimen where the process of grain fracture and void formation has begun, whereas Fig. 11(c) shows fatigue striation marks and deeper fatigue cracks in the area where the fractured grain have been completely dislodged leading to material loss. Thus, plastic deformation followed by work-hardening and fatigue fracture of the grains dominated the material removal mechanisms for CE.

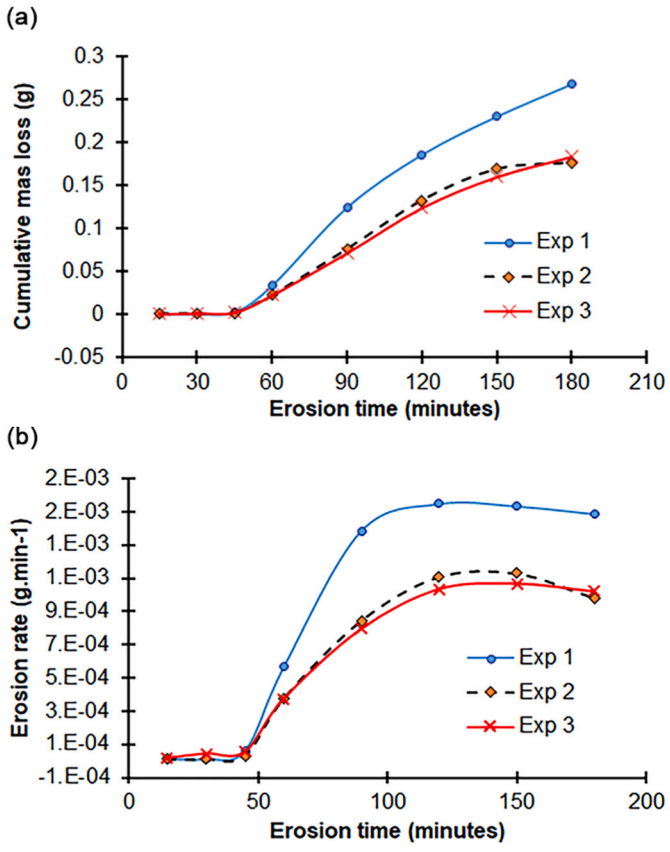

Fig. 9. Cavitation erosion test results (a) Cumulative mass loss measured for Nb with respect of erosion time (b) erosion rate with respect to time.

4. Conclusion

Commercially pure annealed Nb was analysed for its aqueous slurry erosion with the help of an impinging jet apparatus and for its cavitation erosion response with the help of a sonotrode. The following can be inferred from this study:

1. The results revealed the peak erosion rate for an impact angle of 30° and lowest erosion rate for the impact angle of 90° for the conditions employed in this study.
2. Mechanisms such as ploughing, type-1 cutting (due to the sharp edges of impinging erodent particles), and indentation perforation of plastically deformed lips/platelets predominantly participated in material removal at shallow impact angles. Formation of lips/platelets, and breakage of these due to a "plastic deformation-fatigue sequence" and grain boundary cracking leading to grain pull out constituted the dominating material removal mechanism at impact angle of 90°. Thus, this erosion response can be termed as a typical "ductile" behaviour often reported for soft and ductile materials.
3. Four stages of cavitation erosion (CE) i.e, incubation, acceleration, maximum erosion rate, and decelerating erosion rate leading to a near-steady erosion rate were clearly observed in the cavitation studies.
4. Grain boundary sliding and fatigue cracking via intergranular and transgranular cracking of plastically deformed grains following work-hardening effect predominantly participated in material removal in the cavitating conditions.

Results from this work will contribute towards building a fundamental scientific base and will help in decoding erosion-corrosion response of Nb planned in the future studies.

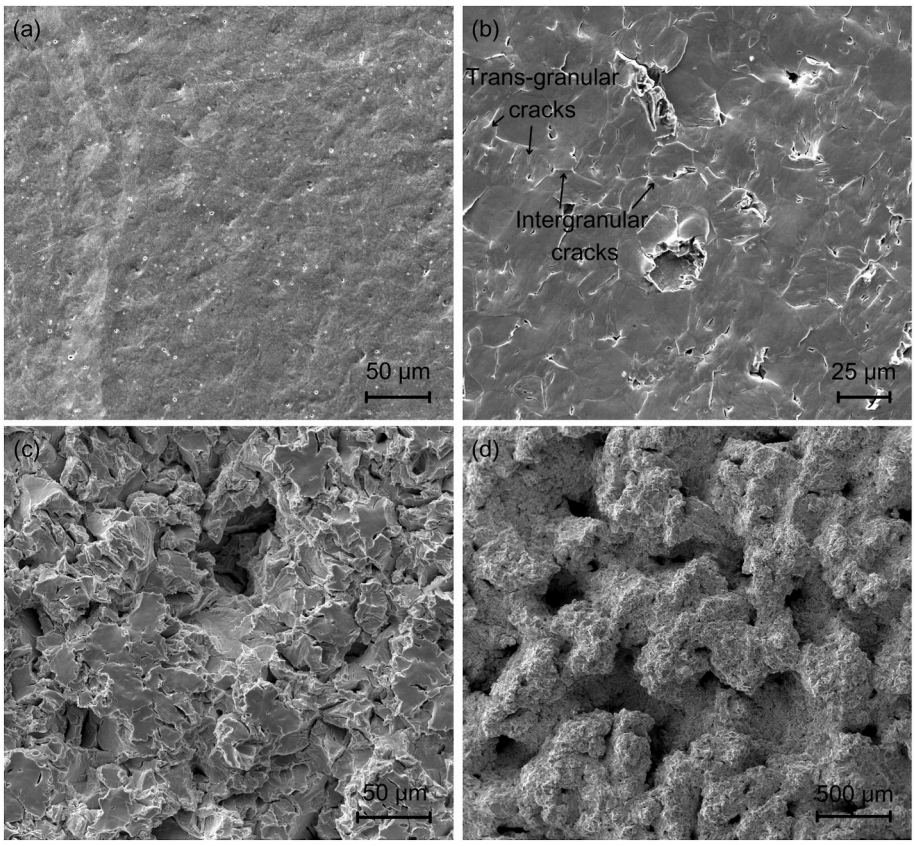

Fig. 10. SEM images of the erosion scar after CE tests with respect to cumulative test time (a) 15 min (b) 45 min (c) 60 min (d) 150 min.

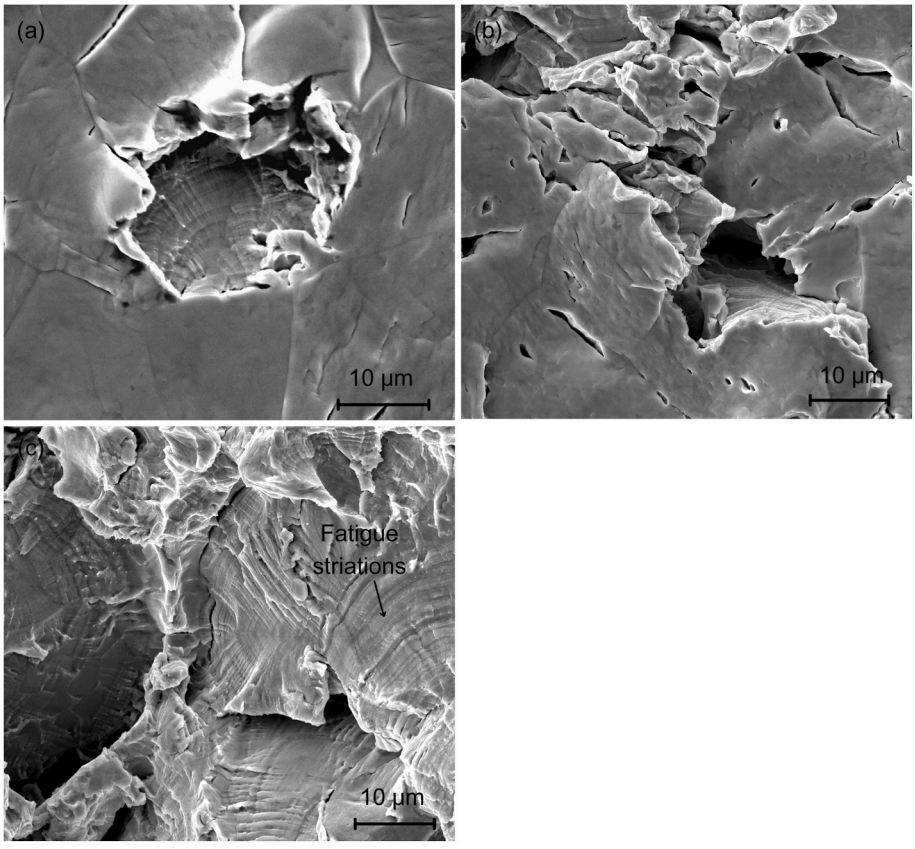

Fig. 11. SEM images of the CE scars: (a) end of 45 min (b–c) end of 60 min.

CRediT authorship contribution statement

H.M.L.U. Madhuwanthi: Writing – original draft, Investigation, Formal analysis, Data curation. **Y.P. Purandare:** Writing – review & editing, Writing – original draft, Supervision, Project administration, Methodology, Investigation, Formal analysis, Data curation, Conceptualization. **A.P. Ehiasarian:** Writing – review & editing, Supervision, Project administration. **A. Dey:** Writing – review & editing, Validation, Supervision, Resources, Project administration, Methodology, Funding acquisition, Conceptualization. **L. Jones:** Supervision, Project administration, Conceptualization. **S. Gallimore:** Supervision, Project administration, Funding acquisition, Conceptualization.

Rights retention statement

"For the purpose of open access, the author has applied a Creative Commons Attribution (CC BY) licence to any Author Accepted Manuscript version of this paper arising from this submission."

Declaration of competing interest

The authors declare the following financial interests/personal relationships which may be considered as potential competing interests:H. M. L. U. Madhuwanthi reports financial support was provided by Rutherford Appleton Laboratory. If there are other authors, they declare that they have no known competing financial interests or personal relationships that could have appeared to influence the work reported in this paper.

Acknowledgements

Financial assistance from Rutherford Appleton Laboratory (RAL), UK for this project is kindly acknowledged. Technical support from Mr. Andrew Gregory, Mr. Robin Sykes (engineering workshop), Dr. Francis Sweeny (electron microscopy) and Dr. Anthony Bell (XRD) from Sheffield Hallam University is much appreciated.

Data availability

Data will be made available on request.

References

[1] Q. Yu, Y. Lu, Z. Hu, B. Zhou, W. Yin, T. Liang, Decay heat calculations for a 500 kW W-Ta spallation target, Nucl. Instrum. Methods Phys. Res. B 351 (2015) 41–45, https://doi.org/10.1016/j.nimb.2015.03.087.
[2] D. Wilcox, P. Loveridge, T. Davenne, L. Jones, D. Jenkins, Stress levels and failure modes of tantalum-clad tungsten targets at ISIS, J. Nucl. Mater. 506 (2018) 76–82, https://doi.org/10.1016/j.jnucmat.2017.10.075.
[3] I.M. Hutchings, P. Shipway, Appendix B: fundamentals of corrosion and tribocorrosion. Tribology, second ed., Elsevier Ltd., 2017, pp. 206–220, https://doi.org/10.1016/B978-0-08-100910-9.09996-7.
[4] J.S. Chouhan, B.D. Jana, Y.P. Purandare, A. Dey, P. Eh Hovsepian, D. Jenkins, L. Jones, Preliminary investigation of slurry erosion bahaviuor of tantalum, Wear 516–517 (2023) 204605, https://doi.org/10.1016/j.wear.2022.204605.
[5] J.S. Chouhan, Y.P. Purandare, B.D. Jana, A. Dey, P. Eh Hovsepian, D. Jenkins, L. Jones, Investigation of aqueous slurry erosion-corrosion behaviour of Tantalum in different pH solutions, Int. J. Refract. Metals Hard Mater. 117 (2023) 106427, https://doi.org/10.1016/j.ijrmhm.2023.106427.
[6] K. Babaei, A. Fattah-alhosseini, R. Chaharmahali, A review on plasma electrolytic oxidation (PEO) of niobium: mechanism, properties and applications, Surf. Interfaces 21 (2020) 100719, https://doi.org/10.1016/j.surfin.2020.100719.
[7] M. Gomez, J. Li, X. Zeng, Niobium: the unseen element – a comprehensive examination of its evolution, global dynamics, and outlook, Resour. Conserv. Recycl. 209 (2024) 107744, https://doi.org/10.1016/j.resconrec.2024.107744.
[8] C.C. Wojcik, Processing, properties and applications of high-temperature niobium alloys, MRS Online Proc. Libr. 322 (1993) 519–530, https://doi.org/10.1557/PROC-322-519.
[9] K.J. Leonard, J.T. Busby, D.T. Hoelzer, S.J. Zinkle, Nb-Base FS-85 alloy as a candidate structural material for space reactor applications: effects of thermal aging, Metall. Mater. Trans. 40A (2009) 838–855, https://doi.org/10.1007/s11661-008-9771-3.
[10] H. Naik, G.N. Kim, K. Kim, M. Zaman, M. Nadeem, M. Sahid, Neutron-induced reaction cross-sections of ^{93}Nb with fast neutron based on ^{9}Be(p,n) reaction, Nucl. Phys. 970 (2018) 156–168, https://doi.org/10.1016/j.nuclphysa.2017.11.011.
[11] J.I. Moench, I. Stephan, A. Koethe, High purity niobium for neutron activation detectors, Mater. Trans. JIM 41 (2000) 67–70, https://doi.org/10.2320/matertrans1989.41.67.
[12] S.F. Brunatto, A.N. Allenstein, C.L.M. Allenstein, A.J.A. Buschinelli, Cavitation erosion behaviour of niobium, Wear 274–275 (2012) 220–228, https://doi.org/10.1016/j.wear.2011.09.001.
[13] G. Bregliozzi, A. Di Schino, S.I.U. Ahmed, J.M. Kenny, H. Haefke, Cavitaion wear behaviour of austenitic stainless steels with different grain sizes, Wear 258 (2005) 503–510, https://doi.org/10.1016/j.wear.2004.03.024.
[14] C.J. Heathcock, B.E. Protheroe, A. Ball, Cavitation erosion of stainless steels, Wear 81 (1982) 311–327, https://doi.org/10.1016/0043-1648(82)90278-2.
[15] R.H. Richman, W.P. McNaughton, Correlation of cavitaion erosion behaviour with mechanical properties of metals, Wear 140 (1990) 63–82, https://doi.org/10.1016/0043-1648(90)90122-Q.
[16] M.M. Stack, Y. Purandare, P. Hovsepian, Impact angle effects on the erosion-corrosion of superlattice CrN/NbN PVD coatings, Surf. Coating. Technol. 188–189 (2004) 556–565, https://doi.org/10.1016/j.surfcoat.2004.07.075.
[17] J.B. Zu, I.M. Hutchings, G.T. Burstein, Design of a slurry erosion test rig, Wear 140 (1990) 331–344, https://doi.org/10.1016/0043-1648(90)90093-P.
[18] I.M. Hutchings, P. Shipway, Wear by hard particles. Tribology, second ed., Elsevier Ltd., 2017, pp. 165–236, https://doi.org/10.1016/B978-0-08-100910-9.00006-4.
[19] I.M. Hutchings, A model for the erosion of metals by spherical particles at normal incidence, Wear 70 (1981) 269–281, https://doi.org/10.1016/0043-1648(81)90347-1.
[20] J.G.A. Bitter, A study of erosion phenomena part II, Wear 6 (1963) 169–190, https://doi.org/10.1016/0043-1648(63)90073-5.
[21] G. Sundararajan, P.G. Shewmon, A new model for the erosion of metals at normal incidence, Wear 84 (1983) 237–258, https://doi.org/10.1016/0043-1648(83)90266-1.
[22] I. Finnie, Erosion of surfaces by solid particles, Wear 3 (1960) 87–103, https://doi.org/10.1016/0043-1648(60)90055-7.
[23] W. Wang, M.J.R. Hache, C. Cheng, Y. Lyu, Z. Liu, M. Papini, Y. Zou, Wear 528–529 (2023) 204971, https://doi.org/10.1016/j.wear.2023.204971.
[24] G.R. Desale, B.K. Gandhi, S.C. Jain, Slurry erosion of ductile materials under normal impact condition, Wear 264 (2008) 322–330, https://doi.org/10.1016/j.wear.2007.03.022.
[25] R. Macchini, M.S.A. Bradley, T. Deng, Influence of particle size, density, particle concentration on bend erosive wear in pneumatic conveys, Wear 303 (2013) 21–29, https://doi.org/10.1016/j.wear.2013.02.014.
[26] I.M. Hutchings, P. Shipway, Wear by hard particles. Tribology, second ed., Elsevier Ltd., 2017, pp. 165–236, https://doi.org/10.1016/B978-0-08-100910-9.00006-4.